Editors' Suggestion

Bichromatic Imaging of Single Molecules in an Optical Tweezer Array

Connor M. Holland,[1] Yukai Lu,[1,2] and Lawrence W. Cheuk[1,*]
[1]Department of Physics, Princeton University, Princeton, New Jersey 08544, USA
[2]Department of Electrical and Computer Engineering, Princeton University, Princeton, New Jersey 08544, USA

(Received 25 August 2022; accepted 4 July 2023; published 4 August 2023)

We report on a novel bichromatic fluorescent imaging scheme for background-free detection of single CaF molecules trapped in an optical tweezer array. By collecting fluorescence on one optical transition while using another for laser cooling, we achieve an imaging fidelity of 97.7(2)% and a nondestructive detection fidelity of 95.5(6)%. Notably, these fidelities are achieved with a modest photon budget, suggesting that the method could be extended to more complex laser-coolable molecules with less favorable optical cycling properties. We also report on a framework and new methods to characterize various loss mechanisms that occur generally during fluorescent detection of trapped molecules, including two-photon decay and admixtures of higher excited states that are induced by the trapping light. In particular, we develop a novel method to dispersively measure transition matrix elements between electronically excited states. The method could also be used to measure arbitrarily small Franck-Condon factors between electronically excited states, which could significantly aid in ongoing efforts to laser cool complex polyatomic molecules.

DOI: 10.1103/PhysRevLett.131.053202

Single molecules trapped in rearrangeable arrays of optical tweezers have been proposed as a platform for quantum simulation, quantum information processing, and precision measurements [1–6]. Compared to the platform of neutral atoms in optical tweezer arrays [7–11], which has been very successful in a wide variety of quantum applications [12–18], polar molecules in tweezer arrays offer new capabilities thanks to their rich internal structure and the long-ranged electric dipolar interactions between them. In particular, molecules in long-lived rotational states within the ground electronic and vibrational manifold can interact with appreciable strengths over micron-scale distances typically found in optical tweezer experiments. In addition, the anisotropic nature of the dipolar interactions enables quantum simulation of many-body Hamiltonians difficult to access with ultracold atoms [1,2]. Recently, experimental efforts have successfully created tweezer arrays with single molecules, either through coherent assembly from their constituent atoms [19–23] or through direct laser cooling [24–26]. In particular, the latter approach promises higher loading rates and detection fidelities required in many applications, because laser-coolable molecules can be directly imaged by repeatedly scattering hundreds of photons. Crucially, this approach could be extended to many more molecules with favorable optical cycling properties, including polyatomic ones [27–31].

Laser-cooled molecules in optical tweezers may be nondestructively detected through fluorescent imaging. However, because of limited tweezer trap depths, cooling is needed to counteract the recoil heating due to photon scattering. To date, Λ imaging [32] has been the only technique that provides both cooling and the fluorescence needed to detect single molecules [24]. Nevertheless, stray laser-cooling light can lead to significant backgrounds that reduce detection fidelities. To circumvent this, one can use two optical transitions, one for laser cooling and the other for inducing fluorescence. Such a bichromatic imaging scheme allows background-free detection since stray laser-cooling light can be spectrally filtered out. This approach has been used to image single atoms in optical lattices and optical tweezers [9–11,33–36]. For molecules, laser-cooled ensembles have been detected bichromatically [31,37], but the more challenging task of detecting single molecules via bichromatic imaging has not been demonstrated.

In this Letter, we propose and realize a bichromatic imaging scheme for high-fidelity detection of single CaF molecules trapped in an optical tweezer array. We also develop a framework and new methods to investigate loss mechanisms encountered generically in fluorescence imaging of trapped molecules.

Bichromatic imaging scheme for CaF.—Our work starts with laser-cooled CaF molecules loaded from a magneto-optical trap [38,39] into a 1D optical lattice formed by a retroreflected 1064 nm laser beam [40]. The molecules are transported to the focus of a high numerical aperture microscope objective (NA = 0.65) and then loaded in the presence of Λ-cooling light into a linear array of 20 identical optical tweezer traps. The tweezer traps are created using focused beams of 781 nm light propagating through the objective along $-\hat{z}$ [Fig. 1(b)]. Each tweezer

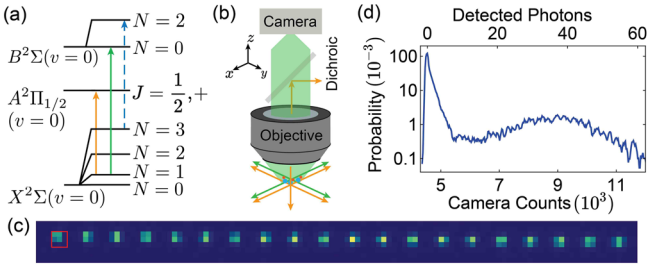

FIG. 1. (a) Relevant CaF levels and transitions used in bichromatic imaging. Shown in orange (green) is the $X-A$ Λ-cooling light ($X-B$ imaging light) at 606 nm (531 nm) used to provide cooling (to elicit $X-B$ imaging photons). Also indicated in blue is light addressing the $X(v=0,N=3)-B(v=0,N=2)$ transition, which is used to address a rotational leakage channel. (b) Λ-cooling light (orange) illuminates molecules along three directions $(\pm\hat{x},\pm\hat{y},\pm\hat{z})$ while $X-B$ imaging light is sent approximately along the $\pm\hat{x}$ and $\pm\hat{y}$ directions. $X-B$ fluorescence (green) enters the objective, passes through dichroic filters, and is detected by an EMCCD camera. (c) Average image of molecules in a 20-site optical tweezer array. The red square indicates an exemplary region for obtaining imaging histograms. (d) Example histogram at an average tweezer occupation of $p=0.21$.

trap has a Gaussian beam waist of $w_0=720(14)$ nm, and has a trap depth of $V=k_B\times 1.28(11)$ mK for molecules in the electronic ground state $X^2\Sigma(v=0)$.

In our bichromatic imaging scheme, we Λ cool the molecules on the $X^2\Sigma(v=0,N=1)\rightarrow A^2\Pi_{1/2}(v=0,J=1/2,+)$ transition at 606 nm, while simultaneously exciting them on the $X^2\Sigma(v=0,N=1,F=0)\rightarrow B^2\Sigma(v=0,N=0)$ transition at 531 nm. Vibrational repumpers addressing the $X^2\Sigma(v=1,2,3,N=1)\rightarrow A^2\Pi_{1/2}(v=0,1,2,J=1/2,+)$ transitions are present. Additionally, light addressing the $X^2\Sigma(v=0,N=3)\rightarrow B^2\Sigma(v=0,N=2)$ transition is applied to repump molecules that decay into $X^2\Sigma(v=0,N=3)$ [Fig. 1(a)]. The resulting $X-B$ fluorescence is collected through the microscope objective and imaged onto an electron multiplying charge coupled device (EMCCD) camera. Dichroic filters in the imaging path remove the Λ-cooling light, $X-A$ fluorescence, and stray optical tweezer light. In detail, the Λ-cooling light is applied along all three directions ($\pm\hat{x}$, $\pm\hat{y}$, and $\pm\hat{z}$), while the $X-B$ excitation light avoids the objective axis ($\hat{z}$) and only propagates roughly in the $\hat{x}$-$\hat{y}$ plane. As shown in Fig. 1(c), the average images obtained using bichromatic imaging reveal the presence of molecules in the tweezer traps. Optimizing for maximal survival at a fixed $X-B$ light intensity of $I=12(1)$ mW/cm^2, we find Λ-cooling parameters similar to those optimal for Λ imaging [24]. We obtain an imaging lifetime of $\tau=148(14)$ ms, and an $X-B$ photon scattering rate of $\Gamma_{\mathrm{sc}}=1.95(4)\times 10^4$ s^{-1}.

Bichromatic imaging performance.—To evaluate the imaging performance, we construct histograms of the total camera counts in cropped image regions surrounding each tweezer [Fig. 1(c)]. The histograms reveal a bimodal distribution [Fig. 1(d)], with the two peaks corresponding to empty and occupied instances. We classify tweezer instances below (above) a threshold θ as empty (occupied), and parametrize the classification errors, ϵ_{10} and ϵ_{01}, the probabilities of incorrectly classifying an occupied tweezer as empty and vice versa, respectively. The total misclassification probability depends on the average occupation p and is given by $\epsilon(p)=p\epsilon_{10}+(1-p)\epsilon_{01}$. We define the imaging fidelity f as the probability of correctly classifying a tweezer when $p=0.5$, i.e., $f=1-\epsilon_{\mathrm{opt}}(0.5)$, at the optimal threshold θ_{opt}. By applying a rescaling procedure to the histograms [41], we obtain the errors ϵ_{10} and ϵ_{01} for 30-ms-long images, from which we extract an imaging fidelity of $f=0.977(2)$ [Fig. 2(a)]. During the images, $\approx$35 photons are collected per molecule, well above the background of $\approx$0.3 photons per tweezer. Our analyses make use of bootstrapping [41], where the data are resampled with replacement and analyzed as independent datasets. This method allows us to obtain error bars without assuming an underlying distribution.

A second imaging metric is the nondestructive detection fidelity f_{ND}, which we define as the probability that a tweezer initially classified as occupied remains occupied following imaging. f_{ND} is given by

$$f_{\mathrm{ND}}=\frac{p(1-\epsilon_{10})}{p(1-\epsilon_{10})+(1-p)\epsilon_{01}}f_{\mathrm{surv}}, \tag{1}$$

where f_{surv} is the survival probability following nondestructive detection. This metric is relevant to rearranging molecules into defect-free arrays, since the success probability of creating an array of size N is limited by $(f_{\mathrm{ND}})^N$. At high survival probabilities and low error rates, $f_{\mathrm{ND}}\approx f_{\mathrm{surv}}-\epsilon_{01}(1-p)/p$. This implies that unlike f, f_{ND} primarily depends on ϵ_{01}, which is approximately the false-positive rate. The detection threshold θ can therefore be increased to reduce ϵ_{01} at the expense of increasing ϵ_{10}, the probability of rejecting occupied tweezers. Because f_{ND} is affected by f_{surv}, the imaging duration should be chosen to balance between minimizing imaging loss and maximizing fluorescence; we find that a 10-ms-long imaging duration strikes this balance.

Experimentally, we measure f_{ND} by taking two consecutive images with durations of 10 ms followed by 30 ms. The fraction of molecules classified as occupied in the second image is corrected using ϵ_{10} and ϵ_{01} to yield f_{ND}. Note that f_{ND} is a property of the first nondestructive image. It is dependent on the classification threshold θ in the first image, but it is independent of the fidelity of the second image. As expected, we find that f_{ND} increases at the expense of rejecting occupied tweezer instances [Fig. 2(b)]. At a moderate data rejection rate of $f_{\mathrm{R}}=15\%$, we achieve a nondestructive detection fidelity of

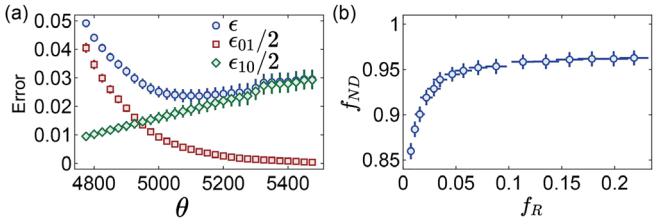

FIG. 2. (a) Error probabilities versus classification threshold θ. Shown in green diamonds and red squares are the measured error probabilities $\epsilon_{10}/2$ and $\epsilon_{01}/2$, respectively. The total error ϵ for an average occupation of $p = 0.50$ is shown in blue circles. ϵ is minimal at an optimal threshold of $\theta_{\mathrm{opt}} \approx 5100$ and corresponds to an imaging fidelity of $f = 0.977(2)$. (b) The nondestructive fidelity f_{ND} (blue circles) versus the data rejection rate f_{R}. Both f_{ND} and f_{R} are controlled by θ. By increasing θ, f_{ND} is improved at the expense of higher f_{R}.

$f_{\mathrm{ND}} = 95.5(6)\%$. Both f and f_{ND} are comparable to or better than previously reported [24,25], and are sufficient for experiments with small-scale rearrangeable tweezer arrays.

We next compare the bichromatic imaging performance to that of single-color Λ imaging. We first examine the dependence of the bichromatic loss rate $\gamma = 1/\tau$ on the $X - B$ imaging power I and find that it increases with I. In particular, the excess loss rate beyond Λ-imaging loss given by $\gamma_{\mathrm{excess}} = \gamma(I) - \gamma(0)$ is observed to increase linearly with I [Fig. 3(a)]. To allow further comparison with single-color Λ imaging, we define a figure of merit $\eta = \Gamma_{\mathrm{sc}}\tau$, where Γ_{sc} is the fluorescence rate of imaging photons, and τ is the imaging lifetime, which encodes how many photons can be scattered before a molecule is lost. At high $X - B$ powers, η saturates to $\approx 3 \times 10^3$, roughly 10 times lower than that of Λ imaging ($\eta \approx 40 \times 10^3$) [Fig. 3(b)]. Hence, Λ imaging is superior if the background from scattered light is identical for both methods. However, in practice, bichromatic imaging performs similarly well because of the significantly reduced background light.

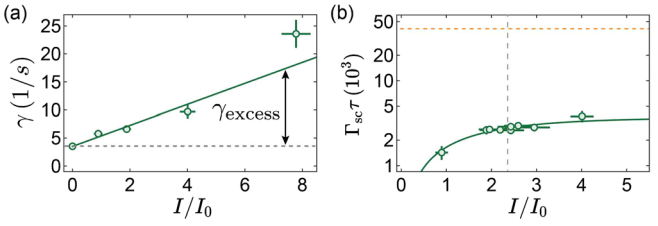

FIG. 3. (a) Green circles show the bichromatic imaging loss rate γ versus the $X - B$ imaging intensity I/I_0 [$I_0 = 5.2(5)$ mW/cm^2]. The solid line shows a linear fit. (b) The figure of merit $\eta = \Gamma_{\mathrm{sc}}\tau$ for bichromatic imaging (green circles) saturates to $\eta \approx 3 \times 10^3$, far lower than that for single-color Λ imaging (orange dashed line, $\eta \approx 40 \times 10^3$). The green curve shows the fit to an exponential saturated curve. The vertical dashed line indicates the $X - B$ intensity used for bichromatic imaging in all measurements. At this intensity, $\eta = 2.7(2) \times 10^3$.

Imaging loss mechanisms.—Loss due to heating: We first examine whether higher molecular temperatures explain the observed excess losses. We perform release-and-recapture thermometry after 100 ms of Λ cooling and bichromatic imaging, and obtain temperatures of 123(20) and 90(20) μK, respectively. The similar temperatures rule out heating-induced loss.

Loss due to rotational branching: We next investigate loss into undetected rotational states, which can be separated into parity-conserving and parity-changing ones. One mechanism of parity-conserving loss arises even under Λ cooling alone. Molecules off-resonantly excited to $A^2\Pi_{1/2}(v = 0, J = 3/2, 5/2, +)$ can decay into $X^2\Sigma(v = 0, N = 3)$ [Fig. 4(a)]. We find that adding a rotational repumping laser addressing the $X^2\Sigma(v = 0, N = 3) \rightarrow B^2\Sigma(v = 0, N = 2)$ transition greatly reduces this to negligible levels. Nevertheless, removing the rotational

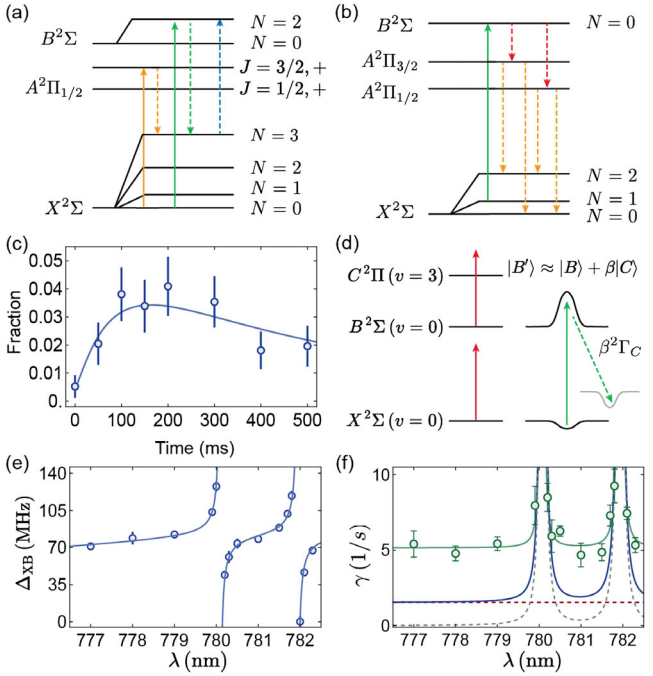

FIG. 4. (a) Parity-conserving rotational loss. Solid arrows show off-resonantly excited transitions. Dashed green and orange arrows show decay channels. The blue arrow indicates the $N = 3$ repumper. (b) Parity-changing rotational loss due to two-photon decay ($B \rightarrow A \rightarrow X$). (c) Detected $X^2\Sigma(v = 0, N = 0, F = 1)$ fraction versus imaging duration at $I = 4.8(4)I_0$. Solid curve shows the fit to a rate equation model [41]. (d) Decay induced by a $C^2\Pi$-state admixture into the $B^2\Sigma(v = 0)$ state. Tweezer light (red) gives rise to repulsive trapping for the $B^2\Sigma(v = 0)$ state by admixing in the near-resonant $C^2\Pi$ states. The dressed state $|B'\rangle$ decays into dark rovibrational states (gray) due to C-state admixture. (e) Δ_{XB} versus tweezer wavelength λ. (f) Excess loss rate γ_{excess} (green circles) versus trapping wavelength λ, at $I = 2.4(2)I_0$. The red (gray) dashed curve shows the estimated parity-changing loss (C-state admixture loss); the solid blue curve is the total estimated excess loss due to both contributions.

repumping laser does not significantly increase γ_{excess} [41]. We note that vibrational-changing loss into $X^2\Sigma(v=1, N=3)$ should be negligible because of the highly diagonal Franck-Condon factors of the $A^2\Pi_{1/2}(v=0) \to X^2\Sigma(v=0)$ and $B^2\Sigma(v=0) \to X^2\Sigma(v=0)$ transitions.

We next quantify parity-changing rotational loss, which could arise from stray electric fields mixing in excited states of opposite parity or molecules decaying via the two-photon pathway $B \to A \to X$ [Fig. 4(b)]. The population admixture of an opposite-parity state due to a small electric field scales inversely with the square of the energy difference. Therefore, the $B^2\Sigma(v=0, N=0)$ state, with a frequency splitting of 20 GHz to the nearest opposite-parity rotational state, is expected to have a much smaller $\mathcal{O}(10^{-3})$ opposite-parity admixture than the $A^2\Pi_{1/2}(v=0, J=1/2,+)$ state, which has a Λ-doublet splitting of $\sim$1 GHz. Because the $X-A$ photon scattering rate is higher than that of $X-B$ light during imaging, while γ_{excess} is comparable to $\gamma(0)$, we can rule out stray electric fields as a cause for loss.

To measure the loss due to two-photon decay, which shelves molecules in the opposite-parity rotational states $X^2\Sigma(v=0, N=0, 2)$, we directly measure the population in $X^2\Sigma(v=0, N=0, F=1)$ versus the imaging duration t. The population initially rises before decaying slowly [Fig. 4(c)]. Using a rate-equation model with independently measured parameters [41], we extract a $B \to A$ branching ratio of $7.9(16) \times 10^{-5}$, slightly lower than the theoretically predicted value of 1.3×10^{-4} [50], but much higher than previously measured in free space in a molecular beam [$9(2) \times 10^{-6}$] [51]. The branching ratio indicates an $A-B$ transition dipole moment of $|d_{AB}| = 0.30(3)ea_0$, $0.07ea_0$ smaller than theoretically predicted [50].

Loss due to admixtures of excited states: Lastly, we investigate loss arising from admixtures of higher-lying C states into the excited B states due to the optical tweezer light. Although the trapping light is far off resonant from transitions involving the ground $X^2\Sigma(v=0)$ state, it is close-detuned to the $B-C$ transitions. Sufficient coupling between the B and C states can lead to observable losses via two mechanisms.

First, strong antitrapping of molecules in the B state can lead to heating and subsequent loss. This antitrapping occurs since the tweezer light is blue-detuned from the strongest $B^2\Sigma(v=0) - C^2\Pi$ ($v=0$, 1, 2) transitions. We have, however, already ruled out heating from our thermometry measurements. Second, admixture of the C state into the B state can lead to decay into unaddressed rotational and vibrational states during imaging, since the C-state admixture can decay via multiphoton pathways and the $X-C$ Franck-Condon factors are nondiagonal [Fig. 4(d)]. To estimate the loss rate due to this pathway, we first use the theoretically predicted value of the $B-C$ transition dipole moment $|d_{BC}^{th}| = 7.33ea_0$ [52], which predicts a loss rate 6 times higher than what we observe. This motivates a careful measurement of $|d_{BC}|$.

A consequence of the large value of the predicted dipole moment $|d_{BC}^{th}|$ is that the polarizabilities of the X and B state differ by a factor of $\sim$20, in addition to differing in sign. Specifically, at the tweezer depth used for imaging, the predicted peak differential ac Stark shift between the X and B states is $\Delta_{XB}^{th} \approx h \times 600$ MHz. This shift is large enough to be probed optically by measuring the optical frequency of $X-B$ light that produces maximal loss. To achieve optical cycling during this measurement, sidebands addressing the four $X^2\Sigma(v=0, N=1)$ hyperfine levels are added to the $X-B$ light [53]. Taking into account trap averaging, we infer a peak differential ac Stark shift of $\Delta_{XB} = h \times 78(2)$ MHz, which is much smaller than Δ_{XB}^{th}, indicating that $|d_{BC}|$ is smaller than predicted.

Next, we keep the tweezer intensity fixed and scan the wavelength of the tweezer light. As shown in Fig. 4(e), Δ_{XB} displays two dispersive features originating from the $B^2\Sigma(v=0) - C^2\Pi_{1/2}(v=3)$ and $B^2\Sigma(v=0) - C^2\Pi_{3/2}(v=3)$ transitions. The amplitudes of the features directly measure $f_{BC,03}d_{BC}^2$, where $f_{BC,03}$ is the Franck-Condon factor between the $B^2\Sigma(v=0)$ and $C^2\Pi(v=3)$ states. Fitting the line shapes and using $f_{BC,03}$ calculated from spectroscopic data [54,55], we find a $B-C$ transition dipole moment of $|d_{BC}| = 2.0(1)ea_0$, much smaller than the predicted value of $|d_{BC}^{th}| = 7.33ea_0$ [52].

Assuming that C-state decays always lead to loss, the C-state admixture into the B state contributes a rate of $\beta^2\Gamma_C P_B$ to γ_{excess}, where β is the amplitude of the C-state admixture, P_B is the excited fraction in the B state, and Γ_C is the C-state decay rate. We determine β from the observed Stark shifts and determine $P_B = \Gamma_{\text{sc}}/\Gamma_B$ using Γ_{sc}, the measured $X-B$ scattering rate, and Γ_B, the B-state linewidth. We estimate Γ_C by assuming that $C^2\Pi$ molecules decay only via E1 transitions, i.e., $\Gamma_C = \Gamma_{C,\text{rad}}$ [41]. Using the measured value of $|d_{BC}|$, along with theoretical values of $|d_{XC}|$ and $|d_{AC}|$, we find a radiative decay rate $\Gamma_{C,\text{rad}}$ of $2\pi \times 5.3(2)$ MHz. The resulting estimated loss rate is much smaller than γ_{excess} [Fig. 4(f)].

Away from the two $B^2\Sigma(v=0) - C^2\Pi(v=3)$ resonances, we only account for $\sim$30% of the observed excess loss rate γ_{excess}. This suggests that either $f_{BC,03}$ is different from that calculated or that additional loss mechanisms exist. The former is unlikely since extensive spectroscopy has been performed on the $X-A$, $X-B$, and $X-C-D$ systems [54,55]. In addition, away from the two dispersive features, the value of Δ_{XB} is weakly sensitive to the $B-C$ Franck-Condon factors and is consistent with our measurement of d_{BC}. This leaves two possible explanations, significant predissociation of certain C states, which would lead to $\Gamma_C > \Gamma_{C,\text{rad}}$, and photoionization of B-state molecules, which could arise, for example, from absorption of an $X-A$ photon and a tweezer photon [56]. The possible

involvement of tweezer light could be probed in the future with rapidly modulated traps, where the temporal overlap of the imaging light and trapping light can be varied [57].

Summary and outlook.—We have demonstrated a background-free bichromatic imaging scheme for single CaF molecules in an array of μm-sized optical tweezer traps. We have achieved an imaging fidelity and nondestructive detection fidelity sufficient for small-scale rearrangeable molecular tweezer array experiments. Crucially, because of our method's background-free nature, only a moderate photon budget of $\eta \sim 10^3$ is required, opening the door for high-fidelity single-molecule detection of complex laser-coolable polyatomic species for which a high degree of optical cycling is much harder to achieve. We note that our technique relies on the presence of two largely closed optical cycling transitions, which has been observed in certain polyatomic molecules [58,59].

While investigating bichromatic imaging loss, we have identified many loss mechanisms generically relevant to fluorescent detection of trapped molecules and have established a framework to systematically quantify their rates. Through these investigations, we have also developed a method to measure transition dipole moments between short-lived excited states, and have performed the first measurement of the $B - C$ transition dipole moment of CaF. This technique could be used to measure arbitrarily small Franck-Condon factors, which could aid in efforts to achieve optical cycling in complex polyatomic molecules [60,61].

We thank John Doyle and his group for fruitful discussions and a careful reading of the manuscript. This work is supported by the National Science Foundation under Grant No. 2207518. L. W. C. acknowledges support from the Sloan Foundation.

*lcheuk@princeton.edu

[1] L. D. Carr, D. DeMille, R. V. Krems, and J. Ye, New J. Phys. **11**, 055049 (2009).
[2] J. L. Bohn, A. M. Rey, and J. Ye, Science **357**, 1002 (2017).
[3] K.-K. Ni, T. Rosenband, and D. D. Grimes, Chem. Sci. **9**, 6830 (2018).
[4] J. A. Blackmore, L. Caldwell, P. D. Gregory, E. M. Bridge, R. Sawant, J. Aldegunde, J. Mur-Petit, D. Jaksch, J. M. Hutson, B. E. Sauer, M. R. Tarbutt, and S. L. Cornish, Quantum Sci. Technol. **4**, 014010 (2018).
[5] P. Yu, L. W. Cheuk, I. Kozyryev, and J. M. Doyle, New J. Phys. **21**, 093049 (2019).
[6] D. Mitra, K. H. Leung, and T. Zelevinsky, Phys. Rev. A **105**, 040101 (2022).
[7] M. Endres, H. Bernien, A. Keesling, H. Levine, E. R. Anschuetz, A. Krajenbrink, C. Senko, V. Vuletić, M. Greiner, and M. D. Lukin, Science **354**, 1024 (2016).
[8] H. Labuhn, D. Barredo, S. Ravets, S. de Léséleuc, T. Macrì, T. Lahaye, and A. Browaeys, Nature (London) **534**, 667 (2016).
[9] A. Cooper, J. P. Covey, I. S. Madjarov, S. G. Porsev, M. S. Safronova, and M. Endres, Phys. Rev. X **8**, 041055 (2018).
[10] M. A. Norcia, A. W. Young, and A. M. Kaufman, Phys. Rev. X **8**, 041054 (2018).
[11] S. Saskin, J. T. Wilson, B. Grinkemeyer, and J. D. Thompson, Phys. Rev. Lett. **122**, 143002 (2019).
[12] M. A. Norcia, A. W. Young, W. J. Eckner, E. Oelker, J. Ye, and A. M. Kaufman, Science **366**, 93 (2019).
[13] T. M. Graham, M. Kwon, B. Grinkemeyer, Z. Marra, X. Jiang, M. T. Lichtman, Y. Sun, M. Ebert, and M. Saffman, Phys. Rev. Lett. **123**, 230501 (2019).
[14] H. Levine, A. Keesling, G. Semeghini, A. Omran, T. T. Wang, S. Ebadi, H. Bernien, M. Greiner, V. Vuletić, H. Pichler, and M. D. Lukin, Phys. Rev. Lett. **123**, 170503 (2019).
[15] I. S. Madjarov, J. P. Covey, A. L. Shaw, J. Choi, A. Kale, A. Cooper, H. Pichler, V. Schkolnik, J. R. Williams, and M. Endres, Nat. Phys. **16**, 857 (2020).
[16] S. Ma, A. P. Burgers, G. Liu, J. Wilson, B. Zhang, and J. D. Thompson, Phys. Rev. X **12**, 021028 (2022).
[17] H. Bernien, S. Schwartz, A. Keesling, H. Levine, A. Omran, H. Pichler, S. Choi, A. S. Zibrov, M. Endres, M. Greiner, V. Vuletić, and M. D. Lukin, Nature (London) **551**, 579 (2017).
[18] S. de Léséleuc, V. Lienhard, P. Scholl, D. Barredo, S. Weber, N. Lang, H. P. Büchler, T. Lahaye, and A. Browaeys, Science **365**, 775 (2019).
[19] K.-K. Ni, S. Ospelkaus, M. H. G. de Miranda, A. Pe'er, B. Neyenhuis, J. J. Zirbel, S. Kotochigova, P. S. Julienne, D. S. Jin, and J. Ye, Science **322**, 231 (2008).
[20] L. R. Liu, J. D. Hood, Y. Yu, J. T. Zhang, K. Wang, Y.-W. Lin, T. Rosenband, and K.-K. Ni, Phys. Rev. X **9**, 021039 (2019).
[21] J. T. Zhang, Y. Yu, W. B. Cairncross, K. Wang, L. R. B. Picard, J. D. Hood, Y.-W. Lin, J. M. Hutson, and K.-K. Ni, Phys. Rev. Lett. **124**, 253401 (2020).
[22] J. T. Zhang, L. R. B. Picard, W. B. Cairncross, K. Wang, Y. Yu, F. Fang, and K.-K. Ni, Quantum Sci. Technol. **7**, 035006 (2022).
[23] S. Spence, R. V. Brooks, D. K. Ruttley, A. Guttridge, and S. L. Cornish, New J. Phys. **24**, 103022 (2022).
[24] L. Anderegg, L. W. Cheuk, Y. Bao, S. Burchesky, W. Ketterle, K.-K. Ni, and J. M. Doyle, Science **365**, 1156 (2019).
[25] L. W. Cheuk, L. Anderegg, Y. Bao, S. Burchesky, S. S. Yu, W. Ketterle, K.-K. Ni, and J. M. Doyle, Phys. Rev. Lett. **125**, 043401 (2020).
[26] S. Burchesky, L. Anderegg, Y. Bao, S. S. Yu, E. Chae, W. Ketterle, K.-K. Ni, and J. M. Doyle, Phys. Rev. Lett. **127**, 123202 (2021).
[27] I. Kozyryev, L. Baum, K. Matsuda, B. L. Augenbraun, L. Anderegg, A. P. Sedlack, and J. M. Doyle, Phys. Rev. Lett. **118**, 173201 (2017).
[28] B. L. Augenbraun, J. M. Doyle, T. Zelevinsky, and I. Kozyryev, Phys. Rev. X **10**, 031022 (2020).
[29] D. Mitra, N. B. Vilas, C. Hallas, L. Anderegg, B. L. Augenbraun, L. Baum, C. Miller, S. Raval, and J. M. Doyle, Science **369**, 1366 (2020).
[30] L. Baum, N. B. Vilas, C. Hallas, B. L. Augenbraun, S. Raval, D. Mitra, and J. M. Doyle, Phys. Rev. A **103**, 043111 (2021).
[31] N. B. Vilas, C. Hallas, L. Anderegg, P. Robichaud, A. Winnicki, D. Mitra, and J. M. Doyle, Nature (London) **606**, 70 (2022).

[32] L. W. Cheuk, L. Anderegg, B. L. Augenbraun, Y. Bao, S. Burchesky, W. Ketterle, and J. M. Doyle, Phys. Rev. Lett. **121**, 083201 (2018).
[33] E. Haller, J. Hudson, A. Kelly, D. A. Cotta, B. Peaudecerf, G. D. Bruce, and S. Kuhr, Nat. Phys. **11**, 738 (2015).
[34] L. W. Cheuk, M. A. Nichols, M. Okan, T. Gersdorf, V. V. Ramasesh, W. S. Bakr, T. Lompe, and M. W. Zwierlein, Phys. Rev. Lett. **114**, 193001 (2015).
[35] R. Yamamoto, J. Kobayashi, T. Kuno, K. Kato, and Y. Takahashi, New J. Phys. **18**, 023016 (2016).
[36] J. Ang'ong'a, C. Huang, J. P. Covey, and B. Gadway, Phys. Rev. Res. **4**, 013240 (2022).
[37] J. C. Shaw, J. C. Schnaubelt, and D. J. McCarron, Phys. Rev. Res. **3**, L042041 (2021).
[38] S. Truppe, H. J. Williams, M. Hambach, L. Caldwell, N. J. Fitch, E. A. Hinds, B. E. Sauer, and M. R. Tarbutt, Nat. Phys. **13**, 1173 (2017).
[39] L. Anderegg, B. L. Augenbraun, E. Chae, B. Hemmerling, N. R. Hutzler, A. Ravi, A. Collopy, J. Ye, W. Ketterle, and J. M. Doyle, Phys. Rev. Lett. **119**, 103201 (2017).
[40] Y. Lu, C. M. Holland, and L. W. Cheuk, Phys. Rev. Lett. **128**, 213201 (2022).
[41] See Supplemental Material at http://link.aps.org/supplemental/10.1103/PhysRevLett.131.053202 for details on experimental procedures and analysis methods, which include Refs. [42–49].
[42] N. R. Hutzler, H.-I. Lu, and J. M. Doyle, Chem. Rev. **112**, 4803 (2012).
[43] H. J. Williams, L. Caldwell, N. J. Fitch, S. Truppe, J. Rodewald, E. A. Hinds, B. E. Sauer, and M. R. Tarbutt, Phys. Rev. Lett. **120**, 163201 (2018).
[44] S. Ding, Y. Wu, I. A. Finneran, J. J. Burau, and J. Ye, Phys. Rev. X **10**, 021049 (2020).
[45] T. K. Langin, V. Jorapur, Y. Zhu, Q. Wang, and D. DeMille, Phys. Rev. Lett. **127**, 163201 (2021).
[46] L. Anderegg, B. L. Augenbraun, Y. Bao, S. Burchesky, L. W. Cheuk, W. Ketterle, and J. M. Doyle, Nat. Phys. **14**, 890 (2018).
[47] Y. Wu, J. J. Burau, K. Mehling, J. Ye, and S. Ding, Phys. Rev. Lett. **127**, 263201 (2021).
[48] T. E. Wall, J. F. Kanem, J. J. Hudson, B. E. Sauer, D. Cho, M. G. Boshier, E. A. Hinds, and M. R. Tarbutt, Phys. Rev. A **78**, 062509 (2008).
[49] P. J. Dagdigian, H. W. Cruse, and R. N. Zare, J. Chem. Phys. **60**, 2330 (1974).
[50] Y. Hao *et al.*, J. Chem. Phys. **151**, 034302 (2019).
[51] S. Truppe, H. J. Williams, N. J. Fitch, M. Hambach, T. E. Wall, E. A. Hinds, B. E. Sauer, and M. R. Tarbutt, New J. Phys. **19**, 022001 (2017).
[52] S. Raouafi, G.-H. Jeung, and C. Jungen, J. Chem. Phys. **115**, 7450 (2001).
[53] C. M. Holland, Y. Lu, and L. W. Cheuk, New J. Phys. **23**, 033028 (2021).
[54] L. A. Kaledin, J. C. Bloch, M. C. McCarthy, and R. W. Field, J. Mol. Spectrosc. **197**, 289 (1999).
[55] C. M. Gittins, N. A. Harris, R. W. Field, J. Verges, C. Effantin, A. Bernard, J. Dincan, W. E. Ernst, P. Bundgen, and B. Engels, J. Mol. Spectrosc. **161**, 303 (1993).
[56] S. F. Rice, H. Martin, and R. W. Field, J. Chem. Phys. **82**, 5023 (1985).
[57] N. R Hutzler, L. R. Liu, Y. Yu, and K.-K. Ni, New J. Phys. **19**, 023007 (2017).
[58] I. Kozyryev, T. C. Steimle, P. Yu, D.-T. Nguyen, and J. M. Doyle, New J. Phys. **21**, 052002 (2019).
[59] G. Lao, G.-Z. Zhu, C. E. Dickerson, B. L. Augenbraun, A. N. Alexandrova, J. R. Caram, E. R. Hudson, and W. C. Campbell, J. Phys. Chem. Lett. **13**, 11029 (2022).
[60] D. Mitra, Z. D. Lasner, G.-Z. Zhu, C. E. Dickerson, B. L. Augenbraun, A. D. Bailey, A. N. Alexandrova, W. C. Campbell, J. R. Caram, E. R. Hudson, and J. M. Doyle, J. Phys. Chem. Lett. **13**, 7029 (2022).
[61] G.-Z. Zhu, D. Mitra, B. L. Augenbraun, C. E. Dickerson, M. J. Frim, G. Lao, Z. D. Lasner, A. N. Alexandrova, W. C. Campbell, J. R. Caram, J. M. Doyle, and E. R. Hudson, Nat. Chem. **14**, 995 (2022).